DOI: 10.61782/fa.2025.0328

FORUM ACUSTICUM EURONOISE 2025

EFFECTS OF BOUNDARY LAYER INGESTION ON DUCTED PROPELLER NOISE

M. Daroukh[1*] **F. Ahmed**[2] **T. Le Garrec**[1]
M. Azarpeyvand[2] **E. Manoha**[1]
[1] DAAA, ONERA, Institut Polytechnique de Paris, 92320 Châtillon, France
[2] Department of Aerospace Engineering, University of Bristol, Bristol, BS8 1TR, United Kingdom

ABSTRACT

In this paper, the effects of boundary layer ingestion on the noise emitted from an academic ducted propeller are evaluated using lattice Boltzmann simulations and wind tunnel experiments. The boundary layer is generated by an aggressive S-plate placed upstream of the propeller and its impact is assessed by comparison with an isolated ducted propeller configuration. Three operating conditions are studied, which correspond to a free-stream velocity of 32 m/s and rotational speeds of 6000, 8000, and 11,000 rpm. Aerodynamic results are compared between simulations and experiments and show a good agreement. They highlight the increase in flow asymmetry and turbulence ingested by the ducted propeller in the presence of the S-plate. Direct acoustic results are extracted from the simulations at the position of the two experimental microphone arrays and compared against experiments in terms of tonal and broadband contributions. Similar trends are observed despite some quantitative discrepancies. In the presence of the S-plate, the stronger flow distortion is responsible for an increase of tonal noise at the blade passing frequencies, while the higher turbulence intensity generates increased broadband noise levels.

Keywords: *ducted propeller noise, boundary layer ingestion, lattice Boltzmann method, wind tunnel experiments*

**Corresponding author*: *majd.daroukh@onera.fr.*

1. INTRODUCTION

In order to reduce aircraft fuel consumption, alternative propulsion systems are investigated, such as open fan [1], distributed electric propulsion [2], or boundary layer ingestion (BLI) [3] architectures. The present paper focuses on the latter configuration, which has been the subject of several concepts of aircraft in recent years [3–5].

The principle of BLI is to minimize the net drag force of the airframe-propulsion arrangement by ingesting and re-energizing the airframe wake through the propulsion system [3]. Some concepts have already shown promising results in terms of fuel savings [5], but they also highlight challenges in terms of noise emissions. In particular, the engines ingest an incoming flow with high turbulence intensity and strong azimuthal mean flow distortion. These characteristics are expected to affect both the tonal and broadband components of the noise emitted by the engines [6, 7].

The present study aims to understand the main mechanisms of noise emission in a BLI configuration by focusing on an academic setup composed of a ducted propeller and a S-plate, as investigated in the European Union's Horizon 2020 ENODISE project (`https://cordis.europa.eu/project/id/860103`). Numerical simulations based on the lattice Boltzmann method (LBM) and wind tunnel experiments are conducted at different operating conditions on this so-called "A2-ducted" configuration. A large database has been generated and is available on Zenodo (`https://doi.org/10.5281/zenodo.14041712`). In this paper, we focus only on a few illustrative results.

The configuration and experimental setup are first described in Sec. 2, before detailing the numerical methodology in Sec. 3. Some aerodynamic results are then pre-

sented in Sec. 4, followed by some acoustic results in Sec. 5. Finally, conclusions are drawn in Sec. 6.

2. CONFIGURATION AND EXPERIMENTAL SETUP

The configuration studied in this paper is composed of a ducted propeller which can be placed above an S-plate to investigate the effects of boundary layer ingestion. The setup, tested in the aeroacoustic wind tunnel facility at the University of Bristol [8], is briefly described below (see the paper of Ahmed *et al.* [9] for a complete description).

The propeller is composed of three blades based on X22A NACA23012 profiles and has a diameter D of 0.254 m. It is placed inside a 0.175 m long duct with inner and outer diameters of 0.255 m and 0.279 m respectively, leaving a tip clearance of 0.5 mm. The position of the propeller inside the duct is such that the distance x_{LE} from the tip leading edge to the duct inlet plane equals $0.0627D$. Three struts are positioned downstream of the propeller to maintain the assembly. Other tip clearance and propeller position values have been tested in the experiments but they are not detailed in this paper. In installed configurations, an S-plate with a total length of 1.69 m and a total width of 1 m is added. It is characterized by an height variation of 0.2 m over a length of 1 m, with a maximum local curvature of 75%. The S-plate is placed in direct continuation of the bottom part of the wind tunnel nozzle. The ducted propeller is located 0.8 m downstream of the nozzle exit plane and touches the plate. As a result, the propeller axis is shifted downwards from the nozzle axis by 0.3 m. The setup in the presence of the S-plate is illustrated in Fig. 1.

In this paper, only one wind tunnel velocity U_∞ of 32 m/s and three rotation speeds N of 6000, 8000 and 11,000 rpm are investigated, but other conditions have been tested experimentally. The three studied regimes are characterized by a tip Mach number M_{tip} of 0.22, 0.33 and 0.44, an advance ratio J of 1.26, 0.94 and 0.69, and a blade passing frequency f_{BPF} of 300, 400 and 550 Hz respectively. These conditions are summarized in Tab. 1.

Many measurements are included in the setup. Pressure taps and microphones are incorporated in the S-plate and hotwire measurements at different axial positions allow an assessment of the flow field development. Regarding acoustics, two farfield microphone arcs are used. One is placed along the plane of the plate (top arc) while the other is in the transverse direction (side arc), as shown in Fig. 1. One microphone is put every 5 degrees but the

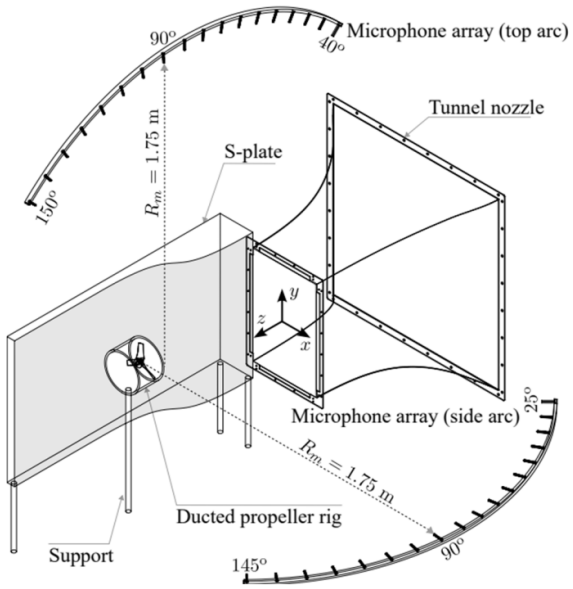

Figure 1. Experimental setup in the presence of the S-plate.

Table 1. Operating conditions investigated in this paper.

U_∞ (m/s)	N (rpm)	M_{tip}	J	f_{BPF} (Hz)
32	6000	0.22	1.26	300
32	8000	0.33	0.94	400
32	11,000	0.44	0.69	550

polar range of the two arcs differ because of installation reasons. The top arc goes from 40 to 150 degrees while the side arc covers the 25-145 degrees range.

3. NUMERICAL METHODOLOGY

In addition to the experiments, numerical simulations based on the lattice Boltzmann method are performed with the *ProLB* solver (`http://www.prolb-cfd.com/`) which is developed by a French consortium composed of universities, research institutes, and industries. The hybrid recursive regularized Bhatnagar-Gross-Krook (HRR-BGK) collision model [10] is used and the lattice is composed of 19 velocities (D3Q19 lattice). The shear-improved Smagorinsky model of Lévêque *et al.* [11] is chosen for turbulence modeling, while the transfer of in-

formation from rotating to fixed parts is managed by an arbitrary Lagrangian-Eulerian approach.

Only part of the setup is included in the simulations for limitation of the computational cost. The isolated cases are thus only composed of the ducted propeller and do not include the wind tunnel nozzle nor the propeller support. The propeller is placed at the center of a cubic fluid domain of size 10 m x 10 m x 10 m. Outlet pressure conditions (with $p_\infty = 101325$ Pa) are prescribed at all external fluid boundaries, except on the one that face the duct inlet where an inlet velocity condition (with $U_\infty = 32$ m/s) is imposed. In order to avoid reflections, absorbing regions are also added close to these external boundaries. Finally, wall boundary conditions (with the use of a wall function) are applied on all solid surfaces. The setup of installed cases slightly differs because it additionally accounts for the S-plate which is assumed to be infinite along its width. The domain is therefore no longer cubic with the replacement of one lateral fluid boundary by the plate. The position of the upstream fluid boundary face is also adjusted to account for the plate length. Note that in order to get a correct boundary layer development over the plate, an artificial plate with a 2 m length is added upstream of the real plate. The first part (1 m) is considered as a frictionless wall while the second part (1 m) is considered as a real wall. A view of the setup defined in installed configurations is given in Fig. 2.

The meshes are done such that the region with the smallest cell size of $\Delta x = 0.1$ mm encompasses the propeller blades, which leaves the place for 5 cells in the radial direction in the tip gap area. The maximum cell size up to the farfield microphones is set to 6.4 mm in order to have least 10 points per wavelength associated to $10 f_{\mathrm{BPF}}$ in the most restrictive case (highest rotation speed), thus allowing for direct noise evaluation. In the installed setup, the plate is added with a prescribed cell size of 0.2 mm in its vicinity. As a result, the isolated setup comprises 500 million nodes and 125 million fine-equivalent nodes (*i.e.* the number of nodes effectively updated at each time step) while the installed setup totalizes 884 million nodes and 330 million fine-equivalent nodes.

The smallest time step is of 168.35 ms, making one full rotation to be described by 59,400, 44,550 and 32,400 iterations at 6000 rpm, 8000 rpm and 11,000 rpm respectively. In all cases, 20 propeller rotations are computed to get converged statistics. The isolated simulations are launched on 1056 processors and last between 60 and 100 h depending on the case, while the installed ones use 2112 processors and last between 100 and 120 h and 100 h. The 11,000 rpm case in installed setup failed to converged, probably because of the appearance of too high local velocities, hardly reachable with such an athermal version of the LBM.

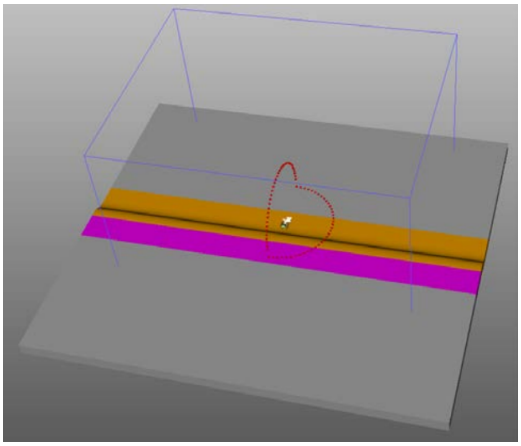

(a) Overview

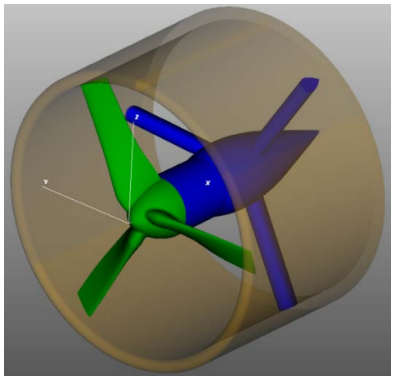

(b) Zoom into the ducted propeller

Figure 2. Numerical setup for installed cases: limits of the fluid domain in blue lines, far field microphones as red dots, real S-plate in orange, artificial upstream plate in purple, blades and spinner in green, hub and struts in blue, duct in transparent orange.

4. AERODYNAMIC RESULTS

Some aerodynamic results are given in this section. The performance map is given for all engine rotation speeds but the flow profiles are only illustrated on the intermediate case ($N = 8000$ rpm) for conciseness, noting that

similar behavior is obtained at other regimes.

We first focus on aerodynamic performance by plotting in Fig. 3 the thrust and drag coefficients obtained in the experiments and in the simulations (averaged value on the last ten rotations). Lines are drawn for experimental results where the wind tunnel speed is varied from 8 m/s to 32 m/s. The points highlight the 32 m/s condition which is the same as the one used in the simulations. For isolated ducted propeller, we observe slightly different operating conditions between experiments and simulations, with an underestimation of both thrust and drag coefficients at all rotation speeds. The tendency is reversed for the installed ducted propeller at 6000 rpm and 8000 rpm where these coefficients are overestimated in the numerical results (recalling that there is no simulation result for the 11,000 rpm case). As a consequence, the effect of BLI on aerodynamic performance (thrust and torque increase) is more marked in the simulations than in the experiments. These observations should be kept in mind when comparing absolute levels between experiments and simulations in the following.

To get an overview of the flow field topology, simulation contour maps of the axial velocity averaged over the last rotation are given in Fig. 4 for both setup at 8000 rpm. In the isolated configuration, the flow is symmetric and we can notice the potential effect of the duct in the vicinity of the inlet plane, as well as the wakes that develop past the hub and duct ends. In the installed case, we clearly see the development of the boundary layer over the plate and its impact with the propeller around $x = 0$ m. The velocity field inside the duct is no longer symmetric as are the duct end wakes. It is interesting to note that the averaged flow velocity ingested by the propeller is slightly lower in the BLI configuration.

In order to provide more insights into the flow field ingested by the propeller, mean and root mean squared (RMS) velocity profiles are extracted at $x = -0.02$ m (just upstream of the inlet plane) and are compared against experiments in Figs. 5 and 6 respectively. We observe a good agreement in both setups in terms of mean flow velocity. In particular, the lobes due to the hub and shroud potential effect are recovered in the isolated case, and the boundary layer development is correctly reproduced in the installed configuration. This result highlights the asymmetry of the mean flow in the presence of the plate. Regarding the RMS profiles, the agreement between simulations and experiments is less good in terms of absolute values, probably because of a small background residual turbulent level in the experiments, but the trends are correctly reproduced. We indeed observe a strong increase of the turbulent levels ingested by the ducted propeller in the installed configurations, especially in the bottom part of the duct.

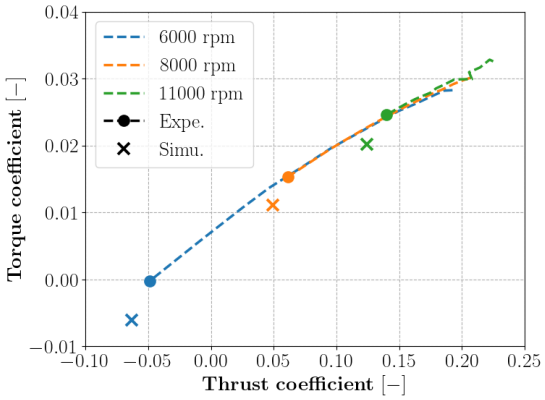

(a) Isolated ducted propeller

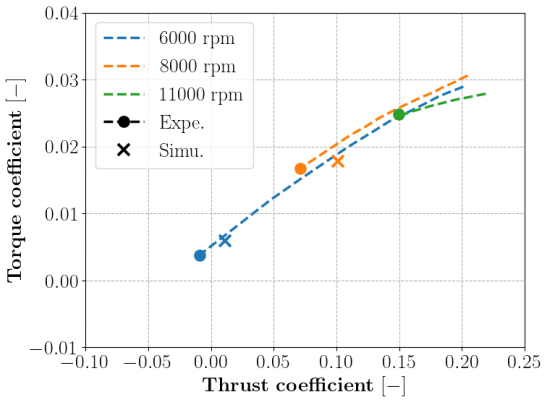

(b) Installed ducted propeller

Figure 3. Thrust and drag coefficients from experiments and simulations. Experimental lines show the evolution for different wind tunnel velocities ($U_\infty = 8 - 32$ m/s), with the dots corresponding to the $U_\infty = 32$ m/s condition.

5. ACOUSTIC RESULTS

The main acoustic results are now provided in this section, by first focusing on the broadband noise and then considering the tonal noise.

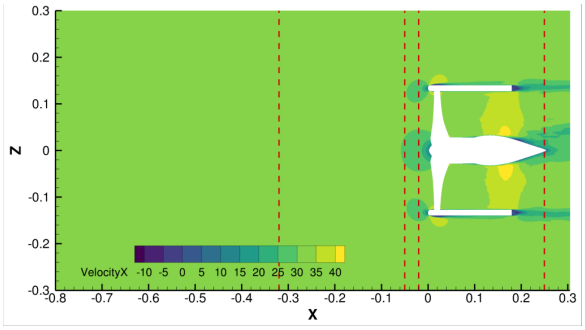

(a) Isolated ducted propeller

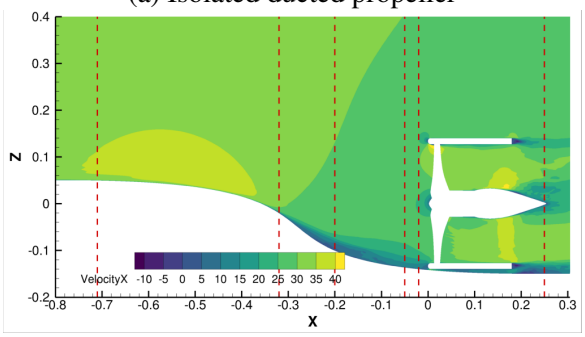

(b) Installed ducted propeller

Figure 4. Contour maps of mean axial velocity obtained from simulations at $y = 0$ m (case $N = 8000$ rpm).

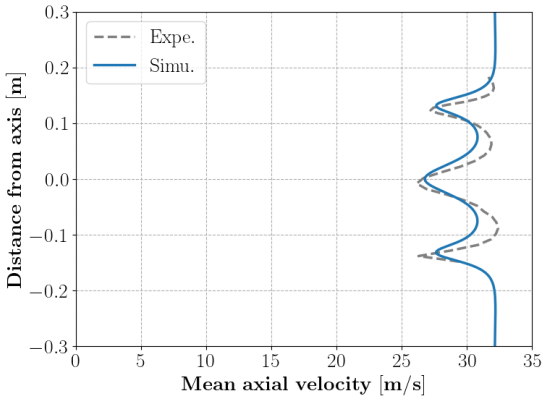

(a) Isolated ducted propeller

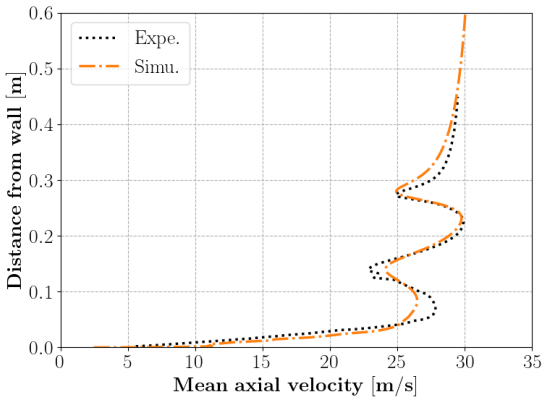

(b) Installed ducted propeller

Figure 5. Mean axial velocity profiles extracted at $x = -0.02$ m from experiments and simulations (case $N = 8000$ rpm).

In order to assess broadband noise, power spectral densities (PSDs) are computed from experimental and numerical time series recorded at the microphones/probes. The time series are first filtered by removing the blade passing phase average in order to remove the tonal component. In the simulations, the PSDs are computed from the last ten rotation signals using the Welch's method with 10 blocks and 50% overlapping. In the experiments, around 30 s of signal (equivalent to $\sim$ 3000 to $\sim$ 6000 rotations depending on the speed) is recorded, thus giving a very small frequency step compared to the numerical one. However, no top tour was included in the setup, which makes the phase average removing quite inefficient. In order to compare broadband noise with a minimal pollution by tonal peaks, only the last ten rotations from experimental measurements are also kept for experimental PSD computations, using again the Welch's method with 10 blocks and 50% overlapping. The tonal component is indeed incorrectly captured in these 10 last rotations because of the engine speed fluctuations, making the tonal contribution much more attenuated. The results for one representative microphone, the one at 90 deg of the side arc (along the propeller plane, see Fig. 1), are given for both setups and for the three rotation speeds in Fig. 7. The low frequencies (lower than $0.5 f_{\mathrm{BPF}}$) are not reliable as there are strong discrepancies between numerical and experimental results, probably because of installation effects in the experiments and/or short statistics in the simulations. In the mid-frequency range (between $0.5 f_{\mathrm{BPF}}$ and 1.5 kHz), the agreement between simulations and experiments is correct, which allows driving some conclu-

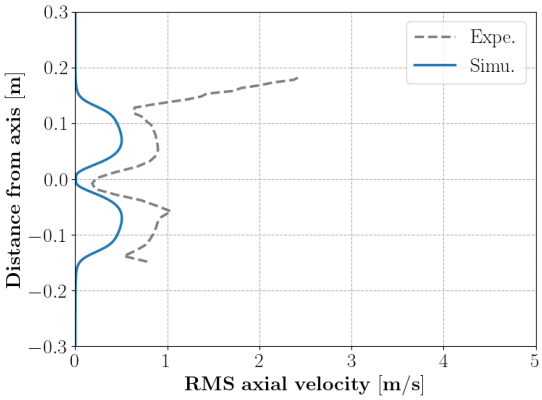

(a) Isolated ducted propeller

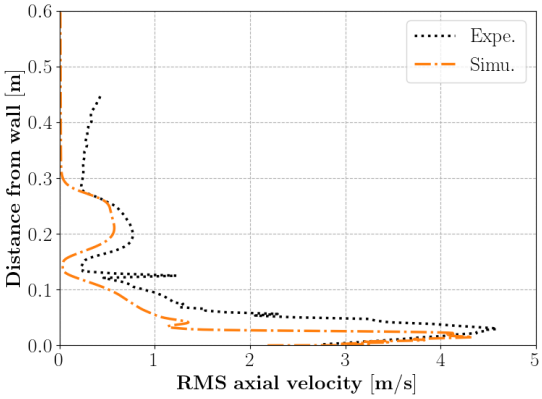

(b) Installed ducted propeller

Figure 6. RMS axial velocity profiles extracted at $x = -0.02$ m from experiments and simulations (case $N = 8000$ rpm).

sions on the effects of BLI. The levels in the installed configurations are indeed much stronger than in the isolated setup, with 10 to 15 dB increase in average. This increase is probably due to the interaction of incoming turbulence with the rotating blades (rotor leading edge noise), which is to be added to the two other main expected broadband noise sources *i.e.* rotor self noise (trailing edge noise) and wakes/struts interaction noise. Above 1.5 kHz, there is a strong mismatch between numerical and experimental levels for the isolated configurations only. Parametric studies performed experimentally (not shown in this paper for conciseness) have shown that this increase is caused by the tip gap noise, a mechanism that is badly captured in the simulations with only 5 points along the radial extent of the tip gap. This noise mechanism seems to be predominant at high frequencies in the isolated setup only. Indeed, in the installed setup, the agreement between experiments and simulations is correct in this frequency range, thus indicating the predominance of the other acoustic sources mentioned above.

The focus is now put on the tonal noise results. The tonal noise is extracted from time signals recorded at the microphones/probes by doing the blade passing phase average over the whole available signals (*i.e.* the last ten rotations in the simulations, and the whole 30 s in the experiments). The directivities of the overall sound pressure level (OASPL) obtained by integrating the contribution from f_{BPF} to $6f_{\mathrm{BPF}}$ are given in Fig. 8. We can observe significant differences in terms of absolute levels between experiments and simulations, with no clear trend. The OASPL is indeed globally overestimated in the simulations at 6000 rpm and 11,000 rpm, while it is underestimated at 8000 rpm. Still, the relative effect of BLI is coherent between measurements and computations, with an average increase of the OASPL by about 10 dB at 6000 rpm and 8000 rpm. There is no simulation for the installed case at 11,000 rpm, but the penalty induced by BLI found experimentally seems to be slightly lower at this condition. This tonal noise increase is to be mainly caused by the propeller unsteady loadings due to the asymmetric flow in the installed configuration (distortion/rotor interaction noise). The other contributors to tonal noise *i.e.* the propeller steady loading and thickness noise and the wakes/struts interaction noise might also be altered by the boundary layer ingestion.

6. CONCLUSION

The effects of boundary layer ingestion are investigated in this paper on an academic setup composed of a ducted propeller that can be placed over an aggressive S-plate. Experiments have been made in the wind tunnel of the University of Bristol and numerical simulations have been performed using the *ProLB* solver based on the lattice Boltzmann method. Many operating points have been measured in the experiments, but we focused in this paper on the three ones that have been considered in the simulations (wind tunnel speed of 32 m/s and propeller rotation speeds of 6000, 8000 and 11,000 rpm). A large database has been generated and is available on Zenodo. Only a few illustrative results have been presented in this paper.

We have shown in particular that the flow ingested by the ducted propeller is largely asymmetric in the presence of the S-plate, which creates an important flow distortion that interacts with the rotating propeller blades. This creates unsteady loading on the blades, an additional source of tonal noise radiation at the blade passing frequencies. The two other main mechanisms, *i.e.* propeller steady loading and thickness noise and propeller-strut interaction noise, might also be altered by the boundary layer ingestion. As a result, the tonal noise levels are significantly increased at all engine rotation speeds, with a 5 to 10 dB penalty.

In addition, the flow ingested by the propeller is also shown to be significantly more turbulent in the bottom part of the duct. The interaction of this turbulence with the rotating blades adds a contribution to broadband noise, which is caused by the rotor trailing edge and tip gap noise and the propeller-strut interaction noise in the isolated setup. The broadband noise levels in the farfield are therefore strongly increased in the presence of the S-plate, with about 10-15 dB in the mid-frequency range. After 1.5 kHz however, the penalty is no more visible in the measurements, probably because of the predominance of tip gap noise. This mechanism is poorly captured in the simulations which explains the discrepancies in this frequency range.

Those results highlight the strong effect of boundary layer ingestion on both tonal and broadband noise. They also show that the tip gap noise is an important contributor to broadband noise in such a setup, which was not necessarily anticipated in the preparation of numerical simulations. Further analyses should be made to better understand the impact of boundary layer ingestion on the different acoustic sources.

7. ACKNOWLEDGMENTS

This work is supported by the European Union's Horizon 2020 research and innovation program through the project ENODISE (ENabling Optimized DISruptivE airframe-propulsion integration concepts) under grant agreement no. 860103.

8. REFERENCES

[1] D. Lewis, C. Perrin, and F. Falissard, "Tonal Noise Predictions of a Generic Open-Fan Based on a Hybrid URANS Approach," in *30th AIAA/CEAS Aeroacoustics Conference*, 2024.

[2] P. Schmollgruber, O. Atinault, I. Cafarelli, C. Döll, C. François, J. Hermetz, R. Liaboeuf, B. Paluch, and M. Ridel, "Multidisciplinary Exploration of DRAGON: an ONERA Hybrid Electric Distributed Propulsion Concept," in *AIAA Scitech 2019 Forum*, 2019.

[3] L. Wiart and C. Negulescu, "Exploration of the Airbus 'Nautilius' engine integration concept," in *31st Congress of the International Council of the Aeronautical Sciences*, 2018.

[4] S. A. Pandya, A. Uranga, A. Espitia, and A. Huang, "Computational Assessment of the Boundary Layer Ingesting Nacelle Design of the D8 Aircraft," in *52nd Aerospace Sciences Meeting*, 2014.

[5] L. Menegozzo and E. Benini, "Boundary Layer Ingestion Propulsion: A Review on Numerical Modeling," *Journal of Engineering for Gas Turbines and Power*, vol. 142, no. 12, 2020.

[6] G. Romani, Q. Ye, F. Avallone, D. Ragni, and D. Casalino, "Numerical analysis of fan noise for the NOVA boundary-layer ingestion configuration," *Aerospace Science and Technology*, vol. 96, p. 105532, 2020.

[7] M. Daroukh, C. Polacsek, and M. Carini, "Acoustic Assessment of BLI Effects on Airbus Nautilius Engine Integration Concept - Part I: Noise Generation," in *28th AIAA/CEAS Aeroacoustics Conference*, 2022.

[8] Y. D. Mayer, H. Kamliya Jawahar, M. Szőke, S. A. Showkat Ali, and M. Azarpeyvand, "Design and performance of an aeroacoustic wind tunnel facility at the University of Bristol," *Applied Acoustics*, vol. 155, pp. 358–370, 2019.

[9] F. Ahmed, I. Zaman, D. Rezgui, and M. Azarpeyvand, "Aeroacoustics of a ducted fan ingesting an adverse pressure gradient boundary layer," *Journal of Fluid Mechanics*, vol. 985, p. R1, 2024.

[10] J. Jacob, O. Malaspinas, and P. Sagaut, "A new hybrid recursive regularised Bhatnagar–Gross–Krook collision model for Lattice Boltzmann method-based large eddy simulation," *Journal of Turbulence*, vol. 19, no. 11-12, pp. 1051–1076, 2018.

[11] E. Lévêque, F. Toschi, L. Shao, and J. P. Bertoglio, "Shear-improved Smagorinsky model for large-eddy simulation of wall-bounded turbulent flows," *Journal of Fluid Mechanics*, vol. 570, pp. 491–502, 2007.

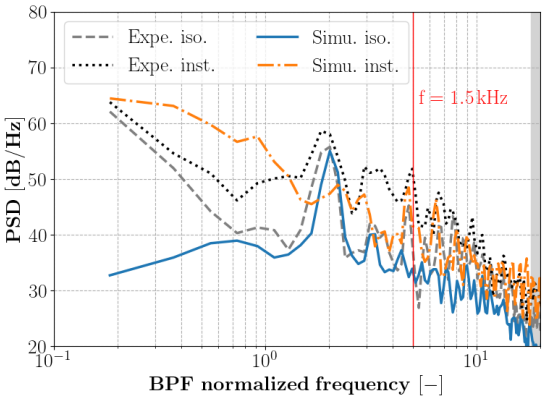

(a) $N = 6000$ rpm

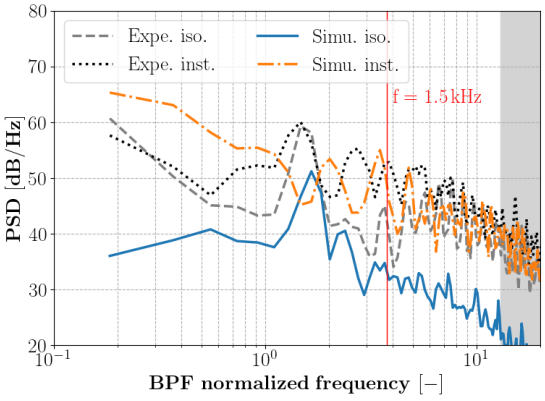

(b) $N = 8000$ rpm

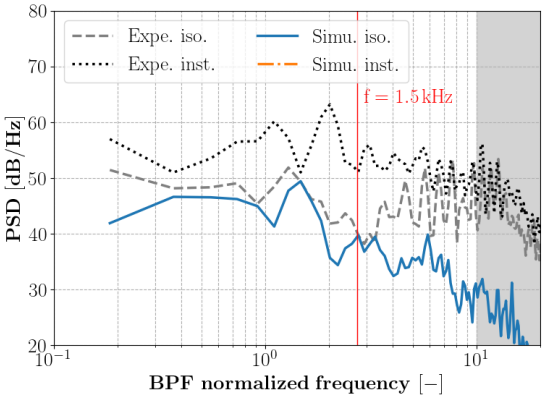

(c) $N = 11,000$ rpm

Figure 7. PSDs computed from experiments and simulations on the 90 deg microphone of the side arc. The grey areas show the mesh cut-off region. The vertical red line highlights the frequency above which the tip gap noise is predominant in isolated setups.

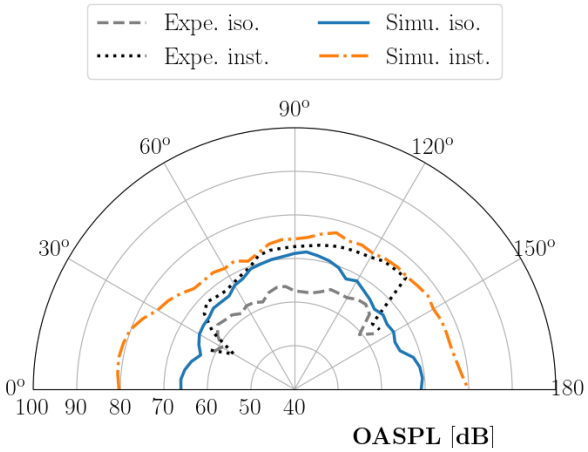

(a) $N = 6000$ rpm

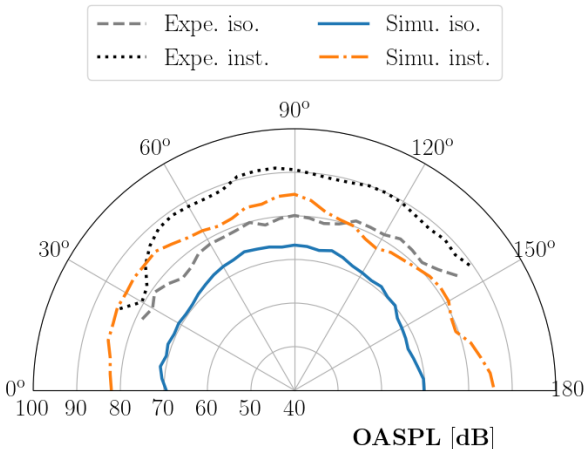

(b) $N = 8000$ rpm

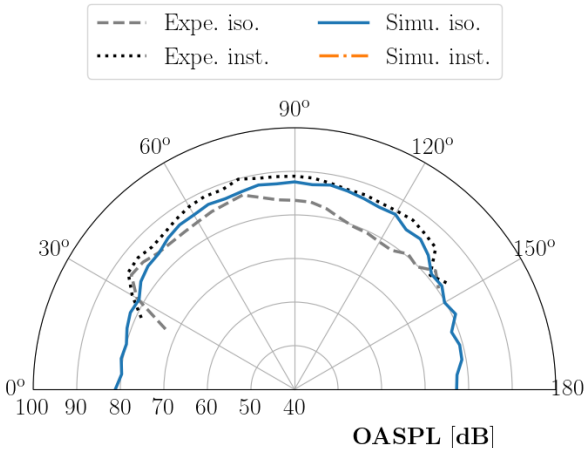

(c) $N = 11,000$ rpm

Figure 8. OASPL directivity over the side arc computed from experiments and simulations by integrating the contribution from f_{BPF} to $6f_{\mathrm{BPF}}$.